Utrecht University

Debye Institute
Nanophotonics group
The Netherlands

Transmission and beam shaping of a Gaussian light beam passing through a dense Rubidium vapour

Author:
Gijs Buist B.Sc.

Supervisor:
Dr. Dries van Oosten

August 2020

Abstract

Laser light can exhibit nonlinear behaviour when interacting with dense atomic vapours. This can give rise to a variety of interesting phenomena such as slow light and optically induced transparency. Recently A. J. van Lange measured nonlinear transmission of light through a Rubidium vapour and developed a physical model to describe these measurements. Van Lange also investigated the formation of different beam profiles, in a dense Rubidium vapour and from Gaussian input beams, as a function of intensity and optical frequency.

Here we expand on van Lange's measurements by measuring over a large frequency range which includes multiple atomic transition lines and by employing off-axis holography which allows for simultaneous measurement of the intensity and phase. Analysis of beam profiles based on the structural similarity index (SSIM) uncovered beam profiles whose path through intensity-detuning space could be described with van Lange's generalised detuning curve. Off-axis holography measurements are in agreement with regular intensity measurements but exhibits a greater amount of noise.

Contents

1 Introduction

In 1960, the first laser was built by Maiman at Hughes Research Laboratories [1]. The great spatial and temporal coherence of laser light sources opened up new avenues of research. Spatial coherence allows laser light to stay narrow over great distances (collimation) and to focus light into a tight spot. The temporal coherence is used to emit light in a narrow spectrum (single colour) or to produce pulses of short duration with a broad spectrum. One of the areas of research that the development of the laser greatly boosted is nonlinear optics. Not long after its invention, nonlinear processes such as two-photon absorption [2] and second harmonic generation [3] were discovered.

Within nonlinear optics, an area of interest is the interaction of intense light with atomic vapours. The combination of high atomic density and high intensity light can lead to a variety of nonlinear effects. For instance, light can be made to propagate in such vapours with a group velocity reduced by several orders of magnitude compared to the velocity of light in vacuum [4, 5]. This reduction in the speed of light to almost zero could lead to the storage of light pulses, which in turn could be of great use in quantum network communication and synchronisation [6, 7]. Other effects include the intensity dependence of the transparency of atomic vapours: opaque vapours can become transparent when excited by an intense laser beam [8, 9]. Additionally, the propagation of the optical field through a nonlinear medium is analogous to the time evolution of a 2D Bose gas [10, 11]. Therefore, relatively simple experiments with nonlinear light could be made to investigate quantum mechanical behaviour that would otherwise require more complex experimental setups. Finally, atomic vapours have shown interesting beamshaping properties. For example the formation of Bessel-Gauss modes, which have self-healing properties, from Gaussian inputs [12], or the formation of size-variable dark-hollow beams [13], which are beams with a doughnut shaped intensity profile with zero intensity in the centre.

Recently van Lange has published work on nonlinear propagation of light in a dense Rubidium vapour [14]. Specifically he measured the transmission of high intensity laser beams on-resonance with an atomic transition of the vapour and constructed a theoretical model which included phenomena such as saturation, optical pumping and collisional depumping. All parameters in the model were calculated from known physical properties, except for the collisional cross section of the Rb atoms in the vapour, which was fitted to the data. Van Lange also found that laser beams with an initially Gaussian shape can be transformed into other, more exotic beams shapes, which depend on vapour density as well as on detuning and on the intensity of the incident light. He identified several characteristic shapes and followed these as a function of detuning and intensity. He found that the resulting curves, with proper scaling, collapsed onto a single curve suggesting that they are caused by the same phenomenon.

The aim of the research of this thesis was to, by expanding upon van Lange's work, construct a setup and methodology that allows for further investigation of nonlinear behaviour of light in a dense vapour. This has been done by building a setup that firstly, is able to probe a larger frequency range, which allows for

the investigation of the effects of multiple transition lines instead of just one, and secondly, by incorporating off-axis holography in the setup, which allows for the measurement of the electric field of the beam, from which both the intensity and phase can be obtained.

In Chapter 2, measurements on the transmission of light through the Rubidium vapour as a function of detuning, intensity and vapour density are presented and, in order to test the functioning of the setup and methods, the results are compared with those of van Lange.

In Chapter 3, measurements made with a setup similar to that of van Lange, on beam shapes formed at the exit of the Rubidium vapour from Gaussian input beams, are discussed and the applicability of the generalised detuning curve found by van Lange is tested both outside of and within van Lange's measurement range.

In Chapter 4, the theory behind off-axis holography is discussed and preliminary measurements with the setup are shown and discussed. Additionally, the transmission measured with this off-axis holography setup is compared with results by the regular intensity setup in order to test the functioning of the new setup.

Finally, in Chapter 5, a conclusion on the research done in this thesis is given, together with recommendations and an outlook for future research.

2 Nonlinear transmission

2.1 Experimental setup

The experimental setup for measuring the transmission through a heated Rubidium vapour is shown in Figure 1. The Rubidium sample consists of a natural mixture of isotopes (78.2% ^{85}Rb, 27.8% ^{87}Rb) in a 10 cm long vapour cell which is wrapped in heating wires, isolated and placed in a heat shield. The temperature of the cell is controlled via the current through the wires and monitored by a thermocouple in direct contact with the cell wall. Light from a fibre coupled diode laser is split, with one part coupled into a wavemeter with which the optical frequency is measured. The other part is sent to a fibre coupled semiconductor optical amplifier (booster) for amplification. After which, the light is out-coupled from the fibre and, using free space optics, sent to a tapered amplifier (TA) to be amplified further. The light beam is then passed through a spatial filter which turns the output of the TA into a Gaussian beam. Next, this beam is split by a pellicle beamsplitter with one part directed to a powermeter and the other into the Rubidium cell. After passing through the cell, the beam is captured on a CCD camera. Neutral density (ND) filters can be attached to the camera to prevent saturation.
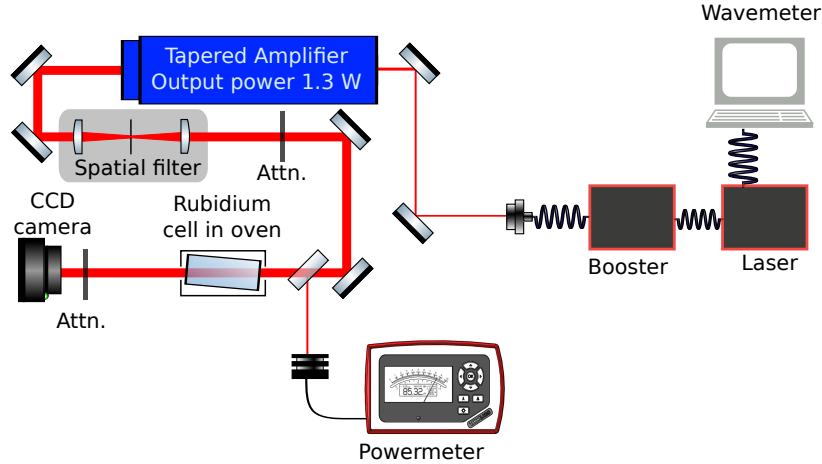

Figure 1: Schematic of the setup for transmission measurements. Important components are the laser diode source, semiconductor optical amplifier (booster) controlled by Thorlabs drivers (CLD 1011 and CLD 1015 respectively), the High-Finesse WS6-600 wavemeter, Toptica BoosTA tapered amplifier and a Point Grey Chameleon camera.

With this setup we wish to measure the transmission of light through the Rubidium vapour as a function of the optical frequency, power of the incident

beam and density of the vapour. We can control the temperature of the vapour via the heating wires and measure it using the thermocouple. This is effectively the same as controlling the vapour density, an increase in temperature increases the density [14]. The optical frequency of the laser diode is controlled by adjusting the current to the laser diode. An increase in current decreases the optical frequency. This process is automated by programming the current of the laser diode driver (Thorlabs CLD 1011) over its USB interface. The power of the incident beam (P_{in}) can be adjusted in two ways: by adjusting the current to either the TA or booster (where an increase in current leads to an increase in power) or by placing ND filters of different strength before the vapour cell. Adjusting the power using ND filters (in our setup) has the disadvantage that the filters have to changed manually, whereas changing the current to the booster or the TA can be done automatically. However, it has the advantage that, when the total attenuation of the ND filters in front of the camera and those in front of the vapour cell are kept constant, the camera does not have to be checked for saturation every time the power is adjusted. We therefore opted to use ND filters to change the power. Figure 2 shows an example of a camera image acquired with the setup.
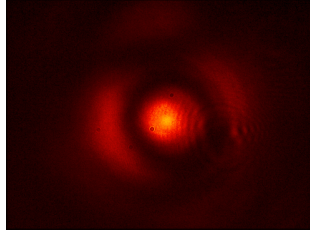

Figure 2: Image captured at T=175 °C, $P_{in} = 304$ mW and at a frequency of 384.2634 THz.

2.2 Analysis

The transmission through the cell is measured by summing the pixels of the image acquired on the camera. The background is first removed by subtracting the average counts of all four 100x100 pixels corners from the image. With this method a transmission spectrum at constant power and vapour temperature can be obtained by increasing the optical frequency in small steps, a single spectrum measurement done this way is called a run. However, the power of the laser source does not remain constant as a function of laser current, and therefore changes with frequency. This change in output power from the laser in turn can cause jumps in the power output of the TA. To solve this we implemented a feedback loop with the powermeter and the TA current. When the powermeter detects a change in power, the amplification of the TA is adjusted such that the power returns to its original value. The results of a run measured with this method are shown in Figure 3a. In this figure, the transmission is normalised
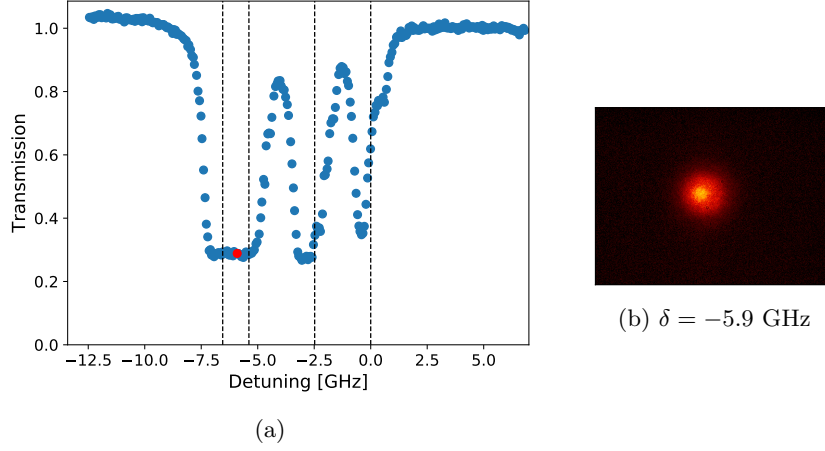
(a)

(b) $\delta = -5.9$ GHz

Figure 3: Left the normalised transmission spectrum measured at T=140 °C and P_{in}=9.3 mW, the red dot indicates the measurement corresponding to the image on the right (b). The black dashed lines are atomic transitions of the Rb vapour.

by setting the transmission far from the (atomic) transition lines to one. The detuning is calculated by defining the optical frequency of 384.23458 THz as a detuning of zero.

We clearly see that the plateaus corresponding to full absorption of the beam have a large offset, suggesting there is a large background that has yet to be taken into account. In Figure 3b the image corresponding to a measurement in the plateau is shown. This image shows that there is still a strong Gaussian signal where total absorption is expected. We attribute this background to amplified spontaneous emission (ASE) which has a broad spectrum and therefore is not significantly absorbed by the vapour. For transmission measurements this offset can be simply set to zero, but for the image itself the removal is not as simple. To remove the ASE a Gaussian is fitted to an image of full absorption which then is subtracted from all of the images of the same run. In case of a run without full absorption a reference image of a run with full absorption taken at the same temperature is used. Since the strength of the ASE is proportional to the power of the incident beam, the reference ASE is multiplied by the power of the run divided by the power of reference run, $ASE_{fit} = \frac{P_{in}}{P_{ref}} * ASE_{ref}$. This effect of the ASE removal on the beam profile of a measurement is demonstrated in Figure 4. A more detailed discussion on ASE and its removal can be found in Appendix A
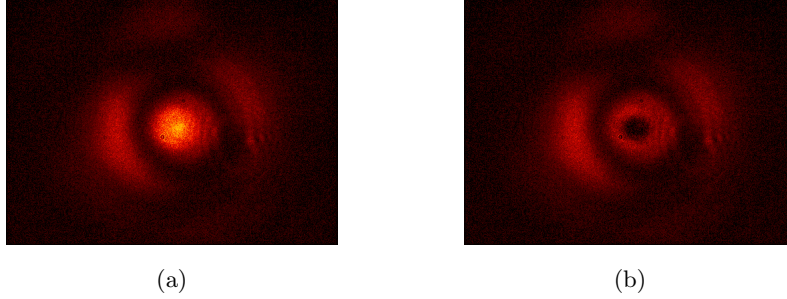
<div align="center">(a)   (b)</div>

Figure 4: (a) shows a frame before ASE removal while (b) is the same frame but after ASE removal. Images have the same normalisation and were captured at T=175 °C, $P_{\mathrm{in}} = 304$ mW and at a frequency of 384.2634 THz.

2.3 Results

Multiple spectra are measured for different P_{in} at the same cell temperature (and hence the same vapour density). Although the same laser currents are used for every run, the optical frequencies at the corresponding measurement points are sometimes shifted due to the limited repeatability of the laser driver. To compare the different runs, we therefore interpolate the transmission values to the same frequency grid. We combine runs with difference values of P_{in} into colour plots. Figure 5 shows such plots for several vapour temperatures. Note that interpolation has been used to create smooth plots. One should be aware that such interpolation can sometimes lead to artefacts.

In these figures, white and yellow indicate high transmission while black and red indicate low transmission. The green dashed lines indicate the atomic transitions in the vapour. The highest frequency transition (384.23458 THz) is defined as a detuning of zero. We see that there is total absorption around the transition lines at low power for all of the vapour densities. As the power is increased the transmission has a sudden increase from zero to non-zero. After this jump the transmission increases more slowly with power until it reaches a high, constant transmission. The power at which this sudden increase happens differs between transition lines and is also dependent on the vapour density. As the temperature/vapour density increases, the jumps in transmission occur at increasingly higher powers. At the highest temperatures (T> 160°) this increase in transmission does not occur at all in our experiments; full absorption can be seen at all powers that we could achieve.

We also see that, as the temperature/vapour density increases, the areas of large/total absorption around the transmission lines become wider. Interestingly, we also note that as the vapour density increases, asymmetric features start appearing. At lower vapour densities we see that at some of the (atomic) resonance lines, there appear minima in transmission on both sides of the resonance line while there is a relative increase in transmission on-resonance. In the colour plots it appears as if the red/dark indicating low transmission are
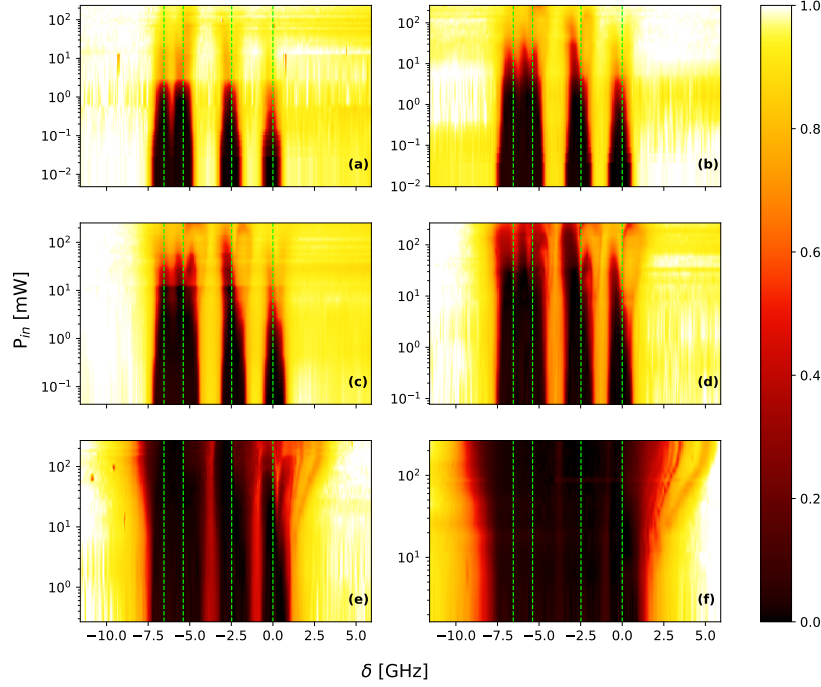
<div align="center">8</div>

Figure 5: Normalised colour plots of the transmission. As the colour bar shows, white indicates full transmission while black indicates full absorption. The green dashed lines indicate transition lines. Each plot was taken at a different temperature; (a) T=87 °C, (b) T=112 °C, (c) T=121 °C, (d) T=140 °C, (e) T=164 °C and (f) T=186 °C,

split in two by the transition line. The minima on the low detuning sides of the resonance lines are deeper compared to those on the high detuning sides. Lastly, at the highest cell temperatures (T=164 °C and up) the absorption area simply becomes wider as the laser power increases, while at the high detuning side of absorption we see the formation of branching lines of high and low transmission.

In order to compare these measurements with those of van Lange, we plot all transmissions at $\delta = 0$ as a function of the saturation parameter s_0. The saturation parameter is given by $s_0 = \frac{I_{\text{peak}}}{I_s}$, where the saturation intensity I_s is 1.6 mW/cm^2 and I_{peak} is given by $I_{\text{peak}} = \frac{2P_{\text{in}}}{\pi w_0^2}$, with P_{in} the incident power and w_0 the waist of the incident Gaussian beam, which is 850 μm in our case. Thus if P_{in} is given in mW, this results in a conversion factor of 35.2, or $s_0 = 35.2 * P_{\text{in}}$. In the experiments done by van Lange, a different laser diode was used, one with an analog current control. To find $\delta = 0$, he tuned the laser diode to find the local minimum in transmission and then recorded that minimal value of the transmission. As we can clearly see from the colour plots in Figure 5, this method does not in fact lead to a constant detuning. Especially in Figure 5(d),

9

it is obvious that the minimum in transmission lies to the left of the resonance for powers above 10 mW.

The way we scan over frequency also leads to complications. As mentioned earlier, the repeatability of the laser current driver is limited. We can therefore not guarantee that we have measured at a detuning of exactly zero. In Figure 6a, the frequency of the measurement closest to $\delta = 0$ for every measurement series is shown. From this we see that most these fall within a range of 0.04 GHz of $\delta = 0$. The average value of the measurements is (by definition) 0 MHz with a standard deviation of 20 MHz.

To get an indication on the sensitivity of the transmission to changes in frequency, we compare transmission measurements for several frequencies close to $\delta = 0$. Specifically, we compare the transmission at frequencies closest and second closest to $\delta = 0$ in both the positive/higher and negative/lower direction. In Figure 6b an example of this for T=101 °C is shown. We see that the general shape of the graph remains the same for the different measurements, but there are significant differences between individual data points at intermediate s_0. Figures for the rest of the temperatures show the same behaviour, which together with the results shown in Figure 6a indicate that comparison with the data of van Lange is reasonable.
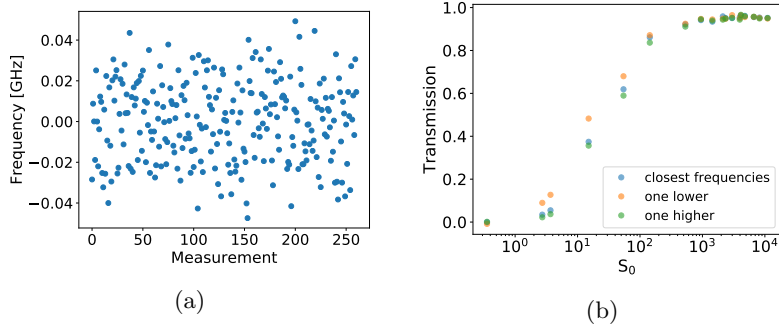

(a)

(b)

Figure 6: In (a) deviation of the measured frequency from the target frequency for all measurements. In (b) transmission at T=101 °C for frequency measurements closest to target frequency (orange), as well as those for one step lower (blue) and higher (green) than those closest to the target frequency.

In Figure 7 the transmission on-resonance as function of the saturation parameter is shown for the different temperatures. At low saturation, the transmission levels are at or close to zero. As the saturation increases there is a point at which the transmission suddenly increases. The saturation parameter at which this happens increases with vapour density. The transmission then continues to increase with saturation until it reaches a (high) value at which it plateaus. The height of these plateaus depends on vapour density, with higher density resulting in a lower plateau.

When compared to van Lange's results, the general shape of the curves is the same except for T=170 and T=185 °C. Here our curves are much flatter
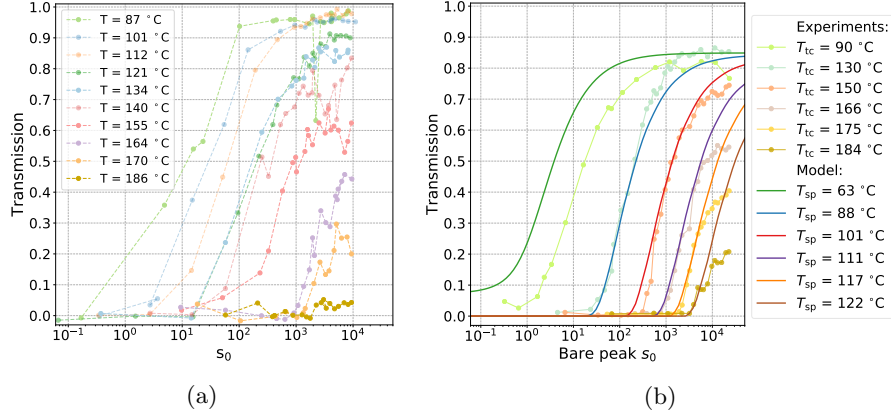
Figure 7: The transmission on-resonance ($\delta = 0$) as function of saturation as measured with our setup (a), in (b) as measured by van Lange. The solid lines in (b) are fits to his model.

than van Lange's.

2.4 Discussion

In Figure 7 we see that the transmission increases suddenly at some saturation after which it keeps increasing until levelling off. Van Lange showed that this behaviour can be explained by taking into account saturation, optical pumping and collisional depumping at the same time, by incorporating these processes in his model which he fitted to the data [14]. The saturation process is strongly dependent on the power or s_0 of the incident beam. As s_0 increases, more and more of the atoms are brought into the excited state. This reduces the amount of atoms in the ground state until at some point there are not enough ground state atoms to significantly absorb photons/light.

In the case of optical pumping, a fraction of the atoms is pumped to an optical dark state. Specifically, atoms that are initially in a hyperfine ground state that is resonant with the incident laser light (bright state) can be excited and subsequently fall back into the another hyperfine ground state that is not resonant with the incident laser light (dark state), therefore reducing the fraction of atoms that can interact with light. The process of optical pumping strongly depends on the saturation parameter (s_0). Finally collisional depumping is a process where transitions between different ground states occur via atom-atom collisions. This has therefore consequences for the fraction of atoms in a dark or bright ground state. If the fraction of dark states is reduced, the fraction of atoms available for light absorption increases. Collisional depumping is strongly dependent on the atomic density, if the density increases the rate of collisional depumping increases.

In Figure 5 we saw that the incident power P_{in} at which the transmission

rapidly increases, increases as the vapour density increases. There are two processes that are affected by density, namely linear absorption and collisonal depumping [14]. For linear absorption, an increase in density leads to an increase in absorption as there more particles to interact with. Collisional depumping, as the name implies, reverses (some) of the optical pumping and its rate increases with density, therefore light absorption is increased as more bright state atoms become available. Thus both processes can contribute to the decrease in transmission as vapour density increases. We also saw in Figure 5 that the areas around the atomic transition lines where total absorption occurs become wider as vapour density increases. This can be caused by what is called collisional or pressure broadening, depending on the field of research. It is an effect where the interaction of one atom with (the mean field) of all surrounding atoms causes a broadening of the linewidth of the atomic transition [15]. Specifically the interaction of one atom with nearby particles affects the lifetime of its excited state(s), when the characteristic lifetime is reduced, the uncertainty in energy associated with the transition is increased. The broadening is proportional to the atomic density. Additionally the broadening affects the saturation intensity (I_s) and therefore the saturation parameter(s_0), this effect is taken into account in van Lange's model.

For the other features in Figure 5, such as the shifting and splitting of transmission minima, branching and the broadening of the absorption area at high powers and vapour densities, we currently have no explanation. Since all these features appear after a certain power and/or vapour density have been reached, it is expected that non-linear processes are involved. Numerical simulations might be used to investigate this behaviour, although such simulations would need to take into account all of the non-linear effects, which is notoriously difficult. Additionally, analysis of beam shapes exiting the vapour cell might help in understanding the physics involved. Analysis of beam shapes is done in Section 3 of this thesis.

Lastly, when comparing on-resonance transmission with van Lange's results, the values for T=170 and T=180 °C van Lange's were significantly higher. The cause of this difference is at this point unclear, and further investigated in Section 3.2.

3 Beam shapes

3.1 Experimental setup

Although measuring beam shapes/profiles is possible with the previous setup, we wish to make comparisons with the work of van Lange on beam profiles, which was done under slightly different conditions. We therefore modified the setup to the configuration in Figure 8. The setup is similar to the setup used for transmission measurements presented in the previous chapter, except for additions that make capturing the Fourier image of the beam exiting the vapour cell possible. These additions include a pellicle beamsplitter, a lens with a focal length f = 100 mm, an iris and an additional CCD camera.
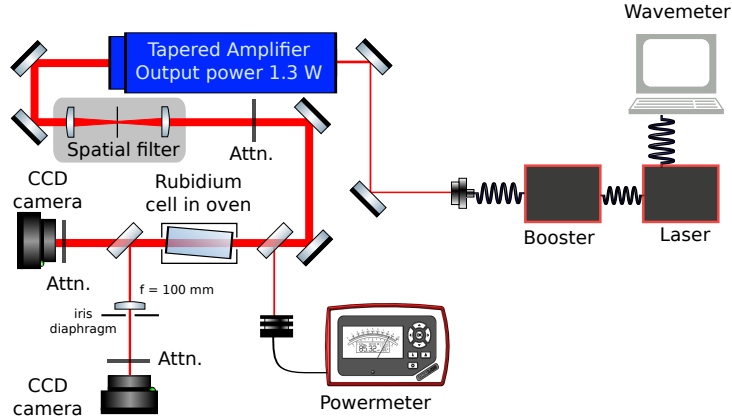

Figure 8: Schematic of setup for beam shape measurements. The configuration is similar to that presented in Figure 1. A beamsplitter, a second camera with lens in 2f configuration and an iris to control the NA have been added.

The (pellicle) beamsplitter is used to redirect part of the beam that exits the vapour cell to the additional camera. The lens is placed after the beamsplitter in a 2f configuration, *i.e.* with both the distance from the vapour cell to the lens and from the lens to the camera equal to its focal length. This forms a Fourier image of the beam exiting the vapour cell onto the camera, which can be compared to the results of van Lange [14]. The iris placed directly after the lens can be used to reduce the numerical aperture (NA) of the image captured on the second camera. In the measurements discussed in this chapter, the iris is fully open unless otherwise specified. An example of images captured this way, after ASE removal following the method discussed previously in this thesis, is shown in Figure 9.
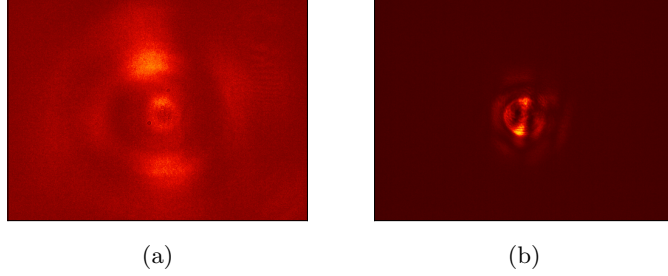
<div style="text-align:center">(a)   (b)</div>

Figure 9: Images taken by the regular (a) and Fourier camera (b). From the same measurement with T=164 $C°$, $P_{\text{in}} = 287$ mW and $\delta = -4.0$ GHz. Images have been normalised separately.

3.2 Transmission spectrum revisited

To verify that the new setup functions properly, transmission spectra were calculated from data captured by both cameras, using the methods described in Chapter 2. The results of these measurements are shown in Figure 10.

In this figure we see that the transmission as measured by the 'regular' camera setup is the same as measured in Chapter 2. However, the transmission measured using the Fourier setup shows significant differences. The Fourier camera measures more transmission in certain regions. Specifically, the broadening at high power and high vapour densities and the branching have disappeared or are strongly reduced. This is especially of interest since these are features for which we could find no immediate physical cause. Also for T=164 °C, top row Figure 10, we see that for the regular camera at high P_{in} the transmission at $\delta = 0$ is higher compared to detunings directly next to it on both sides. The splitting of this transmission minimum is not present in the plot for the Fourier camera and is a feature that appeared at multiple transition lines for T< 164°C in Chapter 2, and were also features for which we had no immediate physical explanation.

Since all conditions before the pellicle are the same for both cameras, the difference in behaviour has to be due to differences in their paths after the pellicle. The differences between the paths are a larger distance from pellicle to camera for the regular camera and a focusing lens in the path of the Fourier camera. Both of these conditions result in a lower numerical aperture (NA) for the regular camera compared to the Fourier camera. It is therefore likely that apparent additional absorption seen with the regular camera but not with the Fourier camera is due to a difference in NA. To test this the NA of the Fourier camera is reduced with the iris to a NA similar to that of the regular camera. The results are shown in Figure 11.

In this figure we see that when the iris leading to the Fourier camera is closed (bottom right image), the features that we observed with the previous setup reappear. This strongly suggests that the branching and broadening are not caused by absorption in the Rb vapour but rather by refraction; the apparent
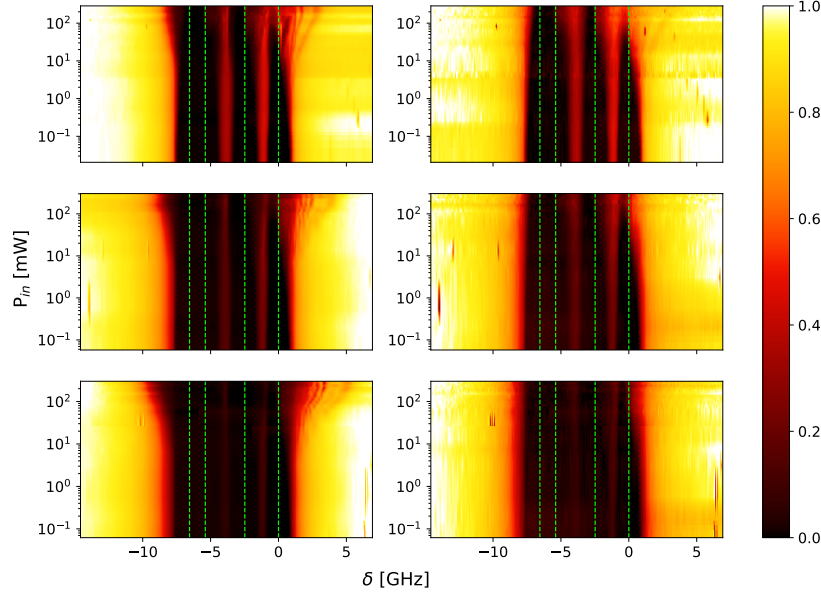
<div style="text-align:center">14</div>

Figure 10: Transmission spectrum colour plots as function of P_{in} and detuning. White/yellow is for high transmission while black/red for low transmission. Dashed green lines show atomic transitions. The left column shows the results from the regular camera while the right column shows those of the Fourier camera, which has a larger NA than the regular camera. Temperatures at every row are equal, from top to bottom: T= 164 °C, T= 175 °C and T= 185 °C.

absorption that is seemingly dependent on the NA is actually due to (part) of the beam falling outside of the NA and thus not being captured on the camera. As for the shifting and splitting of transmission minima, most measurements were done at a vapour temperature that is too high to have such features appear at the probed P_{in} range. However based on the effect that the NA has on such a feature at T=164 °C in Figure 10 we believe that these features are (at least to some degree) also caused by an insufficiently large NA. This is supported by the fact that for detunings close to the transition lines, the areas where in Chapter 2 for lower vapour temperatures we saw shifts and splits in transmission minima, we see that there are beam profiles recorded on the regular camera that do not fit fully on the camera, see Figure 12. To determine with certainty whether or not the size of the NA is solely responsible for the shifts and splits in transmission minima, additional measurements are necessary.

In Figure 13 we take a look at the transmission on-resonance ($\delta = 0$). We see that for high saturation and vapour density, the transmission of the regular camera (cam1) decreases compared to that of the Fourier camera (cam2). This reduction in transmission is in the same region in which our transmission was significantly lower than that reported by van Lange. When the iris is added to
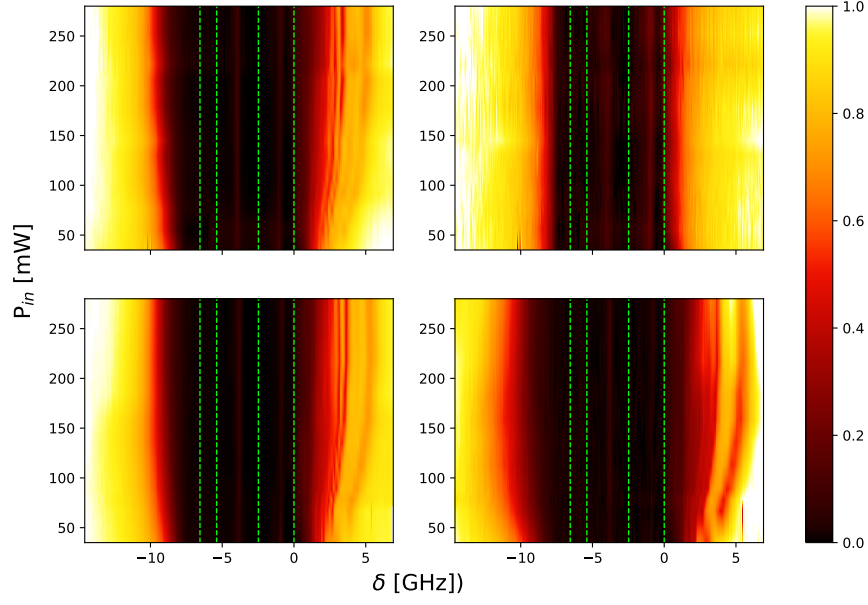
Figure 11: Transmission colour plots. The left column shows transmission measured by the regular camera for cell temperatures of T=185 °C (top) and T=186 °C (bottom). In the right column the corresponding results from the Fourier camera are shown, with the iris open (top) and the iris closed (bottom).
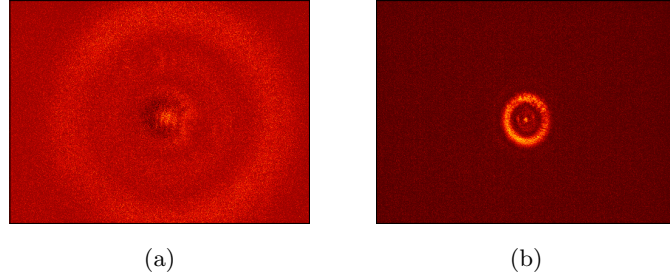

(a)   (b)

Figure 12: Images taken by the regular (a) and Fourier camera (b). From the same measurement with T=164 $C°$, $P_{in} = 160$ mW and $\delta = -3.7$ GHz. Images have been normalised separately.
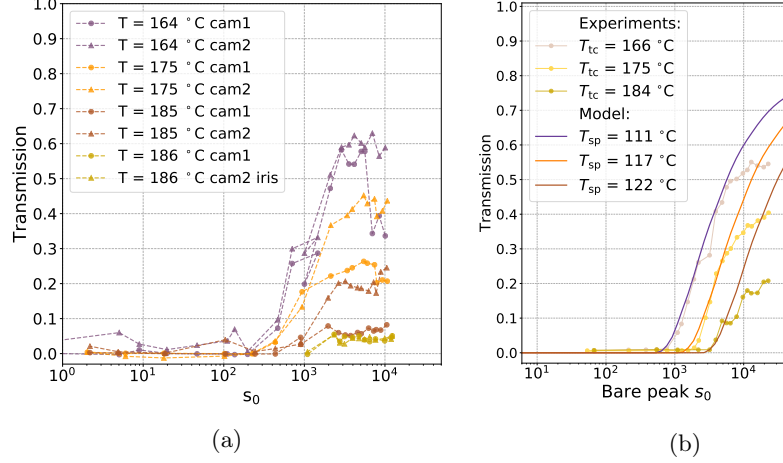
Figure 13: Transmission measurements as function of saturation parameter on-resonance ($\delta = 0$) for different temperatures. In (a) our measurements are shown with cam1 referring to the regular camera and cam2 to the Fourier camera. In (b) van Lange's measurements are shown, with model fits.

the Fourier camera, the transmissions measured using the two different cameras are identical and the disagreement between our results and those of van Lange disappears. Thus we conclude that the earlier measured differences were due to an insufficiently larger NA.

3.3 Analysis

The measurement series for beam profiles are done in the same way as those for transmission described in Chapter 2. A Gaussian beam with constant power P_{in} is sent through the Rb vapour and captured on the cameras, the optical frequency of the beam is then slowly varied as P_{in} is kept constant via a feedback loop. This single spectrum measurement is called a run. We repeat this measurement for several powers P_{in}, resulting in several runs at constant vapour density. After this, the temperature and therefore density of the vapour is changed and when it has stabilised the whole process is repeated.

To compare beam profiles, the ASE and background are first removed from the images, as explained in Chapter 2. Subsequently, each image is normalised by dividing by the highest value. After this the image is cropped to a region of interest. The region of interest is the same for all images and made in such a way that the largest beam profile fills the resulting cropped image. Only images from the Fourier camera are used since, as discussed in the previous subsection, the regular camera does not capture the whole beam at all times due to an insufficient NA.

17

In order to quantify the similarity between two images we use the structural similarity (SSIM) index [16], specifically we use the implementation in the scikit-image package for Python [17]. The SSIM can range between the values of -1 and 1, where 1 indicates identical images, 0 indicates no structural similarity, and negative values indicate that high and low values are inverted in the images.

We compute the SSIM between a selected reference image and all of the images taken at the same temperature. The data is then interpolated the same way as the transmission data was in Chapter 2 to form a colour plot. Figure 14 shows an example result. In the bottom left inset the reference image is shown. The dashed black lines show the atomic transitions of the vapour. Red indicates a high similarity with the reference image while blue indicates a low similarity.
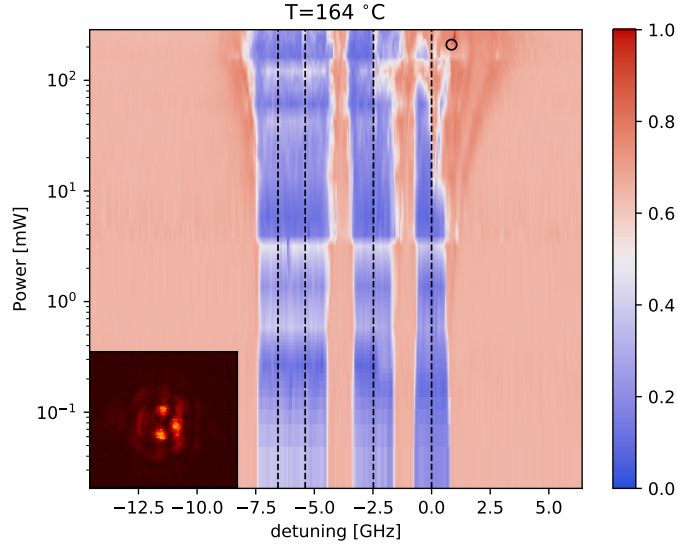

Figure 14: SSIM between the image shown in the left corner with all other images. Red indicates a high similarity with the reference image while blue indicates a low similarity. The black dashed lines indicate the atomic transitions. The reference image was taken at $P_{\mathrm{in}} = 198$ mW and $\delta = 0.8$ GHz, indicated by the black circle.

3.4   Results

Using the methods described in the previous subsection, SSIM plots with a far detuned Gaussian reference beam were made for several temperatures, as shown in the top row of Figure 15. The structures seen in these plots are remarkably similar to the structures seen in the transmission plots for the regular camera, which are shown in the bottom row of the same Figure. The only difference is that for T=175 and T=185°C there are a few horizontal lines of higher SSIM in

a detuning range where there should be total absorption. These features appear due to intensity that remains after ASE removal and not due to physics at the measured optical frequency.
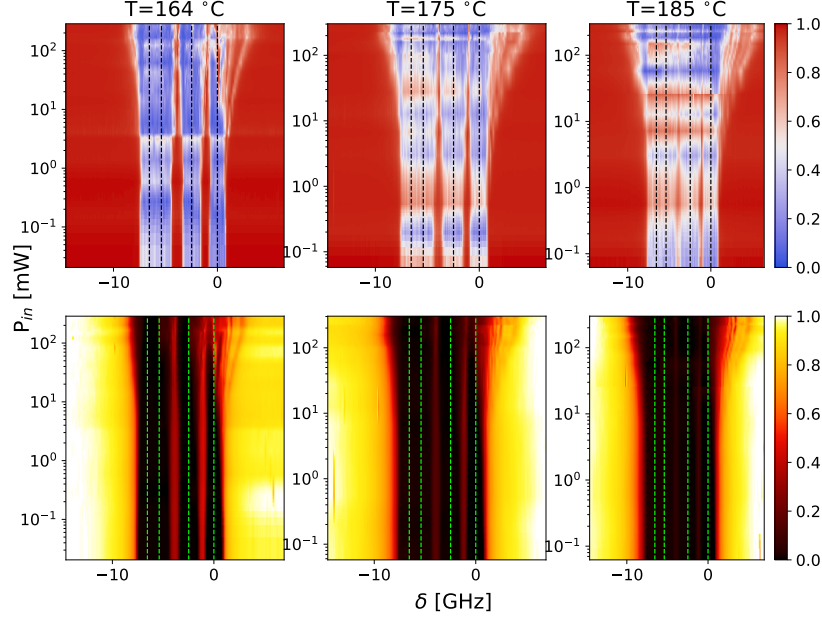

Figure 15: The SSIM of the images based on a Gaussian reference beam (top row), the measurements were taken with the Fourier camera. The bottom row shows the transmission measurements of the regular camera. Each column correspond to a different temperature. In all plots the dashed lines indicate the atomic transitions.

Intensity residues can remain after ASE removal, not only because imperfections in the (Gaussian) fit, but also because the intensity of the ASE is not always equal over the entire run. This can be seen from transmission spectra such as in Figure 3a. Where the height of transmission plateaus at the transition lines are a measure for the intensity of the ASE in those spots. The height of these plateaus can vary slightly and, while not true for the spectrum mentioned above, for some spectra the plateaus even have an small inclination indicating a gradual change in ASE intensity. Since we chose the frame with the lowest peak intensity as reference in the ASE removal procedure, some intensity will remain after ASE removal for measurements where the ASE has increased in intensity.

For the transmission colour plots the slight differences in ASE intensity in a run did not have a significant effect, because the intensity that remained after ASE removal is small compared to the intensity of the input beam. However to compare the different beam profiles we normalised all measurements individually, specifically to ignore differences in intensity between measurements.

Additionally the ASE has the same shape as the Gaussian input beam which makes the profiles that remain after ASE removal show some similarity to a Gaussian. Therefore the Gaussian reference image used shows some similarity to the intensity profiles that remain after ASE removal when the difference in intensity is ignored. While the effect of the imperfect removal of ASE can become apparent in areas where total absorption occurs, the effect outside of this area is limited. This is because the presence of the transmitted beam dominates the beam profile in these cases, as the intensity that remains due to imperfect removal is comparatively small.

In his work, van Lange chose 5 distinct beam profiles in the range of $0 < \delta < 7$ GHz and tracked them through detuning-intensity space. He did this by first defining a reference image for each profile, then at different input powers (P_{in}) he searched for an optimum in the SSIM between the measured profile and the reference image while varying the beam frequency. During the SSIM optimisation process van Lange allowed the measured images to undergo affine transformations such as displacement, rotation, shearing and scaling. This process resulted in a specific detuning curve $\delta_i(s_0)$ for each profile i, see Figure 16a for van Lange's results at T=184 °C.

Van Lange noted that the curves in Figure 16a all showed a remarkable similarity in shape and therefore tried to find a generalised curve on which all the different curves would collapse given a certain normalisation. The formula van Lange used for this normalisation is given by

$$\bar{\delta}_i(s_0) = \frac{\delta_i(s_0) - \delta_{\text{offset}}}{\delta_{i,\text{fin}} - \delta_{\text{offset}}}. \tag{1}$$

Where $\delta_i(s_0)$ is the detuning as function of the saturation for beam profile i, $\delta_{\text{offset}} = 0.850$ GHz and $\delta_{i,\text{fin}}$ the normalisation factor for each profile. Van Lange noted that the detuning curves all seemed to level off and become constant as a function of s_0 at $s_0 > 15000$ (or $P_{\text{in}} > 426$ mW). He used this as basis for the normalisation factor by defining $\delta_{i,\text{fin}}$ as the average of the last three measurement points (the three measurements points at $s_0 > 15000$). Van Lange's normalised curves are shown in Figure 16b, where the black dashed line represents the fit van Lange made to the normalised curves.

The equation van Lange used for his fit is

$$\bar{\delta}_i(s_0) = a + b * s_0^c, \tag{2}$$

and the resulting fit gave $a = -0.12 \pm 0.3$, $b = 0.05 \pm 0.01$ and $c = 0.33 \pm 0.02$. Note that the fit is invalid for $s_0 > 15000$ where the detuning curves become constant as function of s_0, see Figure 16a. Additionally, as beam shape evolution in the Rb vapour is due to nonlinear interactions, there will be no changes in beamshape when the s_0 (or P_{in}) gets below a certain value. Therefore there exists a $s_{0,\text{min}}$ beneath which the generalised detuning curve is no longer valid.

In Figure 15 we see that the SSIM colour plots (top row) have (curving) branches of equal SSIM in the $0 < \delta < 7$ GHz region. These curves of equal SSIM are believed to indicate curves with a constant beam profile and their
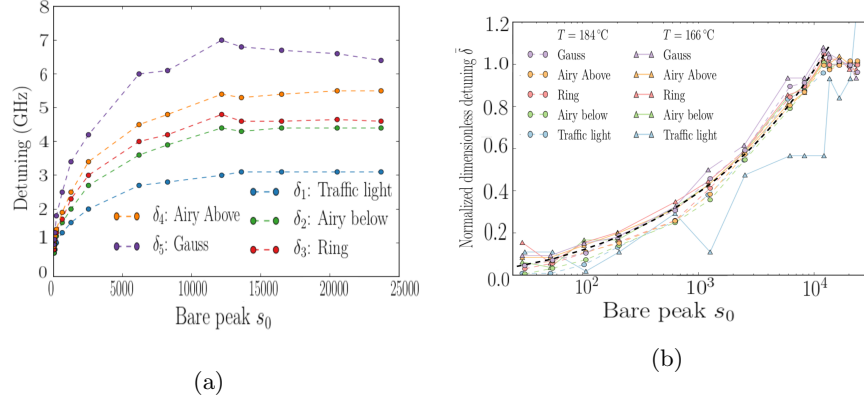
Figure 16: Van Lange's measurements on beam profiles. In (a) the detuning curves of 5 characteristic shapes at T=184 °C. In (b) normalised detuning curves on a logarithmic, normalised with Eq.1. The black dashed line indicates a fit to the curves, the 'Traffic light' (blue triangles) beam at T=166 °C was not included in the fit.

shape is reminiscent of van Lange's detuning curves. To test this, we decided to use van Lange's generalised detuning curve to determine specific detuning curves of characteristic beam profiles close to or on these branches. To determine the specific detuning curves we used:

$$\delta_i(s_0) = (\delta_{i,\text{fin}} - \delta_{\text{offset}})\bar{\delta}_i(s_0) + \delta_{\text{offset}}, \tag{3}$$

where $\bar{\delta}_i$ and δ_{offset} are taken from van Lange's work. Since the normalisation factor $\delta_{i,\text{fin}}$ is determined by measurements at $P_{\text{in}} > 426$ mW, which is outside of our range, we needed to determine it in a different way. We determined the normalisation factor by first inspecting the beam profiles in the area of interest. Several beam profiles were assumed to be characteristic of a specific detuning curve ($\delta_i(s_0)$). The s_0 and δ at which those characteristic beam profiles were measured could then be plugged in Eq.3 to calculate the normalisation factor ($\delta_{i,\text{fin}}$) of each specific detuning curve. Thus all parameters of Eq. 3 are known and it could be used to calculate the specific detuning curves. The calculated curves were drawn for $s_0 > 10$ (or $P_{\text{in}} > 0.284$ mW) since visual inspection of the images showed that only Gaussian profiles are present below this threshold. The results are shown in the top row of Figure 17 and the beam profiles used in Figure 18.

The calculated curves drawn in the top row of Figure 17 seem to closely follow the features in the SSIM plots, except for a curve drawn at T=164 °C. This is the curve closest to the transition line and the only curve that curves toward the transition line instead of away from it. Also, this curve is the only curve for which the detuning (δ) of the image used to calculate the curve is smaller than δ_{offset}.
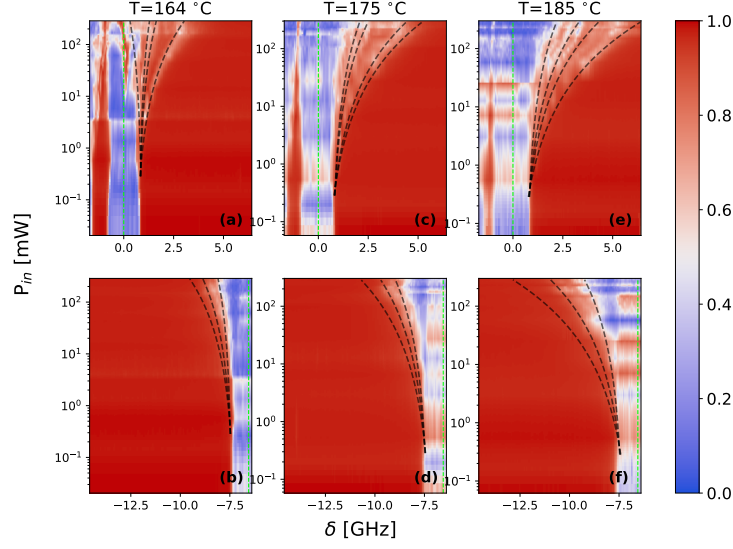
21

Figure 17: Calculated SSIM for images from the Fourier camera with a Gaussian reference image. The green dashed lines indicate atomic transitions while the black dashed lines are calculated detuning curves. The top row shows the positive detuning side while the bottom row shows the negative detuning side. The columns have equal vapour temperature.

Previously we only considered data within the same frequency range as van Lange's measurements. However, as we measured over a larger frequency range, we were interested to see if behaviour similar to that of van Lange's detuning curves can be identified outside of the $0 < \delta < 7$ GHz region. In Figure 15 we can see that no features exist in the frequency range between the transition lines which are of a similar shape as van Lange's generalised detuning curve. However in the area on the negative detuning side of all of the transition lines we see that the border between high (red) and low (blue) SSIM seems to have a similar shape as the detuning curves. Before detuning curves can be calculated in this area, a new δ_{offset} has to be determined. This was done by reading off from the SSIM plots, at P_{in} close to zero, the detuning at the jump between the high and low SSIM. This resulted in $\delta_{\text{offset,left}} = -7.49$ GHz. The normalisation factor $\delta_{i,\text{fin}}$ was determined the same way as was done for the positive detuning side, the area of interest was searched for characteristic beam profiles and their measurement points were used to calculate their corresponding specific detuning curve. The beam profiles that were used are shown in Figure 19 and the detuning curves calculated as a result are shown in the bottom row of Figure 17.

In Figure 17 we can see that in each plot on the bottom row the two detuning curves closest to the transition line seem to follow the border between high and low detuning. The detuning curve furthest from the transition line in the different plots does not correspond to features in the SSIM plots. The
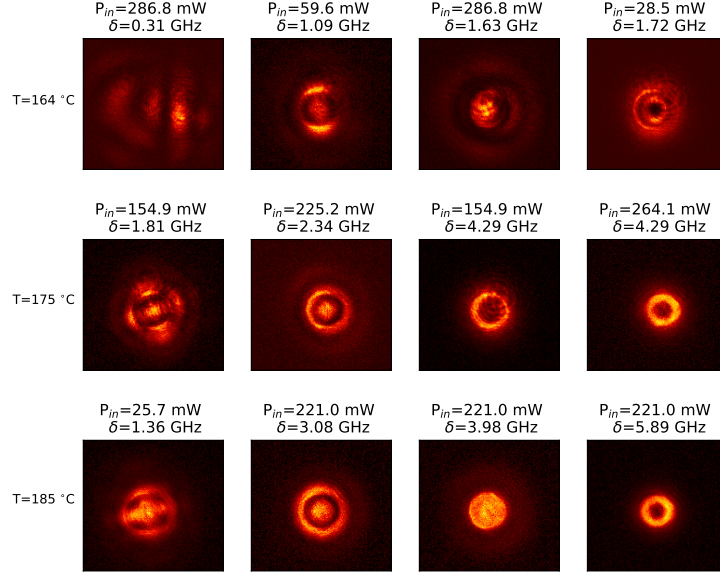
22

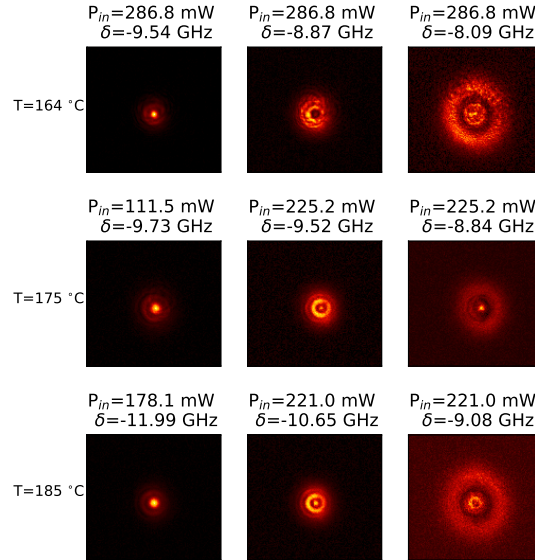Figure 18: Images used to fit detuning curves on the positive detuning side.

Figure 19: Images used to fit detuning curves on the negative detuning side.

characteristic beam shape used to calculate this detuning curve in the different plots is a Gaussian that has been focused compared to the input beam with a diffuse low intensity disc surrounding the (focused) Gaussian profile. The SSIM method seems to attach a high similarity between the profiles just described and a Gaussian profile causing them to be indistinguishable with this method. Therefore a different methodology would need to be used to test if the detuning curve calculated based on these specific beam shapes describes their actual path through detuning-intensity space.

Finally there is the frequency range between the two offsets ($-7.49 < \delta < 0.85$ GHz), where there are no features visible which can be described by van Lange's generalised detuning curve. In this area beam shapes often change rapidly and many seemingly random patterns are formed, examples of which are shown in the top row of Figure 20. Other shapes that appear are rings of different sizes, as can be seen in the bottom row of the same figure. The plots on the bottom row show low similarity between the reference images and the rest of the beam profile measurements. This is in disagreement with visual inspection of the beam profiles, where beam profiles measured close to the reference images show similar patterns with a single ring or multiple rings. This discrepancy is likely caused by the relative strength of the noise in the images, which is due to high absorption of the input beam, see reference images bottom row Figure 20.
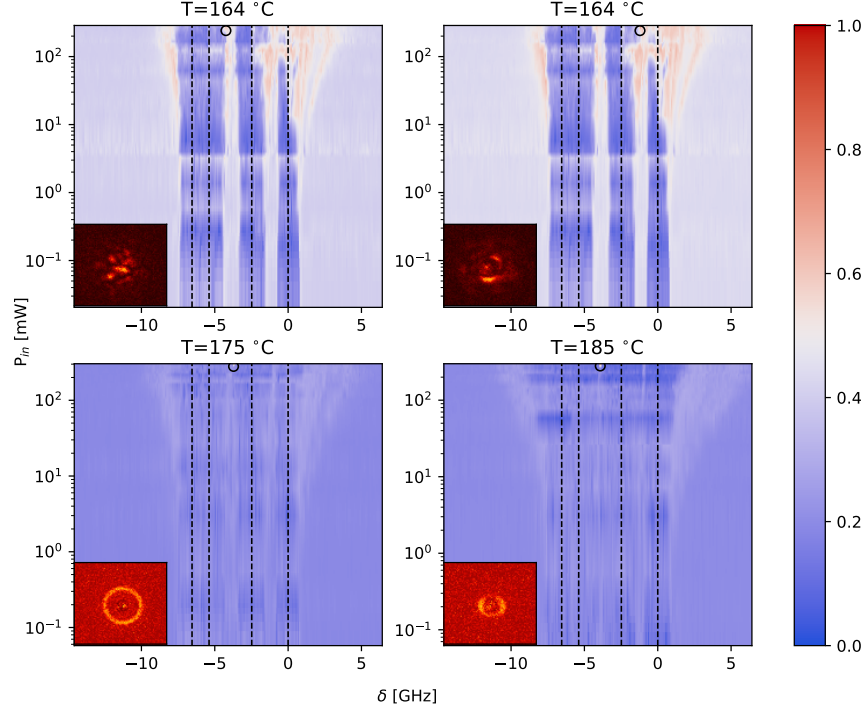
Figure 20: Graphs show the calculated SSIM for the Fourier camera measurements, with the used reference image shown in the bottom left of every graph. The black dashed lines indicate atomic transitions. The black circles indicate the position of the reference image in the plot.

3.5 Discussion

In Chapter 2.2 we found features in the transmission spectra which we could not link to any absorption process in the Rb vapour. In this Chapter, we found that these apparent losses in transmission were not in fact due to absorption in the Rb vapour, but rather due to the fact that the beam shapes generated by the Rb vapour showed strong refraction, causing some light to fall outside of the NA of the camera. These features therefore disappear when the NA is large enough. The refraction also affected the comparison with van Lange's data, causing transmission measured at high vapour density and power to be significantly lower when compared to van Lange's measurements. The transmission measurements of the camera with a large NA were in good agreement with van Lange's measurements.

The similarity between a Gaussian beam profile reference and all other beam profiles was calculated via the SSIM method. The plots created from the calculated similarity showed remarkable similar features when compared with the transmission plots of the low NA camera. The similarity between features in

25

the SSIM and those in the transmission for the low NA further supports our conclusion that the NA-dependent transmission features are linked to strongly refracting beams.

To compare our beam profile measurements with those of van Lange we used the generalised detuning curve fitted to his data to calculate specific detuning curves for some characteristic beam profiles. This was done for both detunings on the positive side of the transition lines, the area where van Lange's generalised detunig curve was fitted, and on the negative detuning side of the transition lines, where van Lange's generalised detuning curve had to be adapted. Some of the calculated detuning curves show a reasonable overlap with features on the SSIM plots, in the area of positive detuning the SSIM features that overlapped with the calculated detuning curves were branching lines and in the negative detuning area the feature was the border between high and low detuning. The agreement between these SSIM features and calculated detuning curves suggest that the features in the plots indeed describe lines of constant beam profile and that the beam profiles used to calculate the detuning curves are characteristic for their calculated curve.

Then there are the beam profiles for which the calculated detuning curve does not correspond to features in the SSIM plot. The lack of agreement between the calculated detuning curves and features in SSIM plots can be due to SSIM method, if it cannot distinguish between beam profiles we do consider different, then no features specific to this beam profile can be seen. Lack in agreement between measurements and the calculated detuning curves can also be due to physical effects, the physics which dictates beamshape can change due to the proximity of multiple transition lines, or by simply getting very close to atomic resonance. This would mean that the generalised detuning curve description is no longer valid in those cases. Issues with the SSIM method are believed to be the cause in case of the detuning curve calculated for the beam profiles of a focused Gaussian surrounded by a diffuse disc. Since for the SSIM method the previously mentioned beam profiles are indistinguishable from Gaussian profiles and therefore even if the focused Gaussian profiles lie on a line described by the generalised detuning curve they get lost in a sea of 'regular' Gaussian profiles.

While van Lange's generalised detuning curve works well when a single transition line dominates the physics, it seems no longer applicable when multiple transition lines are involved. The SSIM method is also not very useful to investigate the different speckle patterns that form under these conditions. This is because the structural similarity index is developed to mimic human perception which is not well suited to characterise speckle patterns. As for the ring patterns that form in the area between the different transition lines, the signal to noise ratio is too low to apply the SSIM method.

To learn more about the detuning behaviour of these noisy or speckly patterns, machine learning techniques could be explored.

4 Off-axis holography

4.1 Theory

Holography is a technique which is used to record the electric field of the wave front of light using an interference pattern [18]. This can be done physically on special photographic plates, from which the full 3-dimensional light field of the recorded object is emitted when it is illuminated with a reference beam. It can also be done digitally, by recording the interference pattern using a digital sensor array. The captured interference pattern can then be used to compute the light field of the recorded object [19, 20].

There are several methods for creating and recording interference patterns which encode the hologram. In our setup we use digital off-axis holography. This is based on a reference beam, approximated as a plane wave, which is overlapped under an angle with the signal beam we wish to measure, see Figure 21. The reference beam and signal beam are derived from the same source and therefore have the same optical frequency.
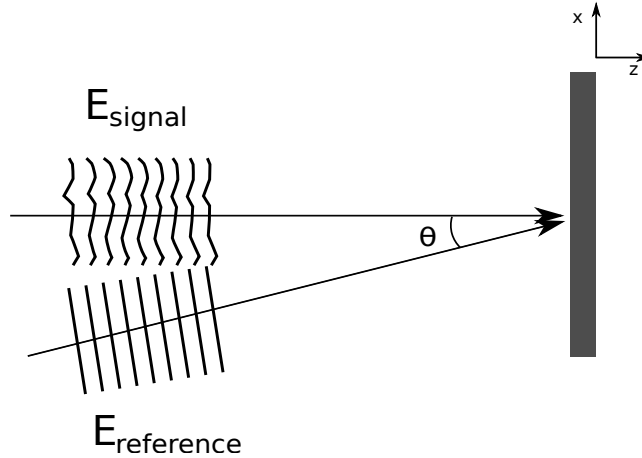

Figure 21: A schematic drawing of the off-axis holography method.

The intensity measured as a result of the interference of these beams is, ignoring prefactors, given by

$$I = |E_\mathrm{s} + E_\mathrm{ref}|^2 = |E_\mathrm{s}|^2 + |E_\mathrm{ref}|^2 + E_\mathrm{s}^* E_\mathrm{ref} e^{ikx \sin \theta} + E_\mathrm{s} E_\mathrm{ref}^* e^{-ikx \sin \theta}, \quad (4)$$

where E_s and E_ref are the electric fields of the signal and reference beams, respectively and θ is the angle between the beams, while k is the wavenumber. The first two terms on the right hand side of the equation are the intensity of the signal and reference beam, respectively, while the last two terms represent the interference.

If the interference pattern is recorded digitally on a camera, the electric field of the signal beam can then be retrieved numerically. First the Fourier

transform of the recorded image is computed. This results in three peaks in the Fourier signal due to the following property of the Fourier transform

$$\mathcal{F}(E_\mathrm{s}E_\mathrm{ref}^*e^{-ikx\sin\theta})(\bar{k}) = \mathcal{F}(E_\mathrm{s}E_\mathrm{ref}^*)(\bar{k}+k\sin\theta), \tag{5}$$

where k is the wavenumber as mentioned earlier and $\bar{k}$ is the new variable in Fourier space. Thus if $k\sin\theta$ is large enough, three fully separated objects corresponding to the zeroth order (terms with no complex exponential), -1 order (terms that go with e^{-i}) and 1 order (terms that go with e^i) can be seen.

In order to correctly measure the periodic behaviour in the -1 and 1 order terms, the Nyquist-Shannon sampling theorem needs to be satisfied. This states that in order to reconstruct a periodic signal from discrete samples the sampling rate has to be at least twice per period of oscillation. Thus, for a signal with period P, the sample rate S needs to satisfy $S \geq \frac{2}{P}$. The period of a complex exponential is 2π, thus the distance between two samples Δx has to be such that

$$k\Delta x\sin\theta \leq \pi. \tag{6}$$

The sample distance is determined by the pixel size, which for our case gives $\Delta x = 3.75\mu\mathrm{m}$. This means that the maximum angle between the signal and reference beam is given by

$$\theta_\mathrm{max} = \arcsin\frac{\lambda}{2\Delta x}. \tag{7}$$

For light with a wavelength $\lambda \approx 780$ nm this gives $\theta_\mathrm{max} = 5.97°$.

If an angle θ can be found which satisfies Nyquist-Shannon, while also having a large enough separation between the orders in Fourier space, the different orders can be filtered out. For example, we can take the area around the -1 order and set all values outside of this area equal to zero. Applying the inverse Fourier transform to this will then get us only the -1 order term of the signal. Furthermore if we shift the signal around the -1 order in Fourier space to the origin before applying the inverse Fourier transform, the exponential term drops out. This leaves us with $E_\mathrm{s}E_\mathrm{ref}^*$ (or $E_\mathrm{s}^*E_\mathrm{ref}$ for the 1 order) which then can be divided by $|E_\mathrm{ref}|$ which in turn can be acquired via a separate measurement. This yields the reconstructed electrical field of the signal beam from which different quantities such as intensity and phase can be determined.

4.2 Experimental setup

The experimental setup for off-axis holography measurements is shown in Figure 22. The setup is similar to the previous setup with the addition of a reference beam for off-axis holography. The reference beam is created by outcoupling part of the light from the fibre coupled diode laser and sending it through a telescope. This results in a Gaussian beam with a large waist, that can effectively be considered a plane wave. This beam is then redirected by several mirrors to be overlapped under a small angle with the signal beam onto a CCD camera. Neutral density filters are used to control the intensity of the reference beam.
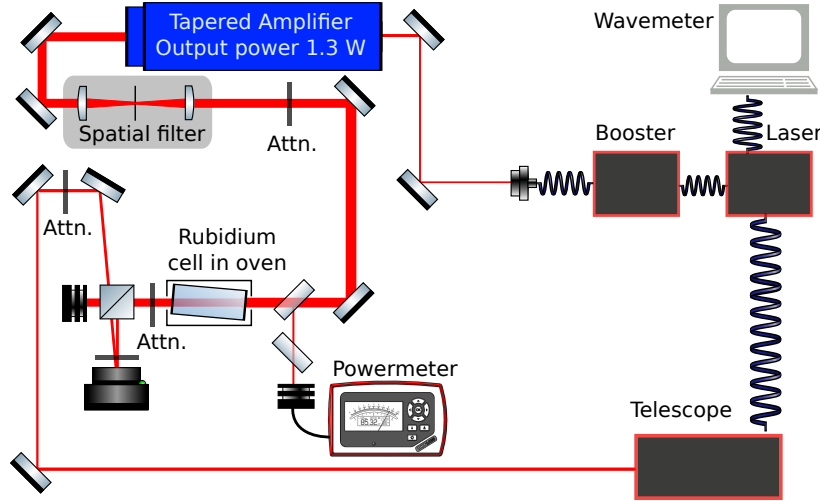
Figure 22: Schematic of the off-axis holography setup. A telescope is used to blow the Gaussian signal from the laser up into approximate plane waves.

Another change is that ND filters, used to control the strength of the beam after the vapour cell, are placed directly after the cell instead of directly in front of the camera. This is done in order to control signal and reference beam strengths separately as they enter the camera. The pellicle beamsplitter is replaced with a cube beamsplitter, as acoustic vibrations of the pellicle caused large fluctuations in the interference pattern. Lastly, as off-axis holography yields both amplitude and phase, it is not longer useful to acquire on two different camera. Instead a single camera (without a lens) close to the cell is used.

4.3   Analysis

Every measurement series or run starts with a measurement of the reference beam with the signal blocked. The signal is then unblocked and using the methods described in Chapter 2.2 the interference pattern is measured as function of the optical frequency while keeping power and vapour temperature constant. The image of the reference beam measured at the start is subtracted from the measured interference patterns. Because the power of the laser changes slightly with the supplied current (and therefore with the optical frequency), the peak signal of the reference beam has to be rescaled for different frequencies. In the case of the direct laser diode output, the relation between beam power and frequency turns out to be linear, making the rescaling simple. The nonlinear behaviour we noticed in the previous chapters is thus fully due to the behaviour of the optical amplifiers, which are not used in the reference beam path. Figure 23 shows the results of such a subtraction. Due to damage on the telescope lenses there are some deformations in the reference beam as can be seen in Fig-

ure 23a. However, as long as interference pattern and the aberrations do not overlap, the aberrations are removed by the subtraction mentioned earlier, as demonstrated in Figure 23b. Still, since the shape and size of the signal beam, and therefore the interference pattern, change during runs, non-overlap is not guaranteed. It is therefore important that for future measurements that these telescope lenses are repaired or replaced.

<div align="center">(a)   (b)</div>

Figure 23: The left image (a) shows the full interference pattern of a measurement. The right image (b) shows the same image but with the reference beam, as measured at the start of the run, removed after rescaling.

After subtracting the reference beam, the results are Fourier-transformed, resulting in an image with three peaks: the -1 order, the 0th order and the 1 order. The position of the peak of the -1 order is determined from a measurement done with a large detuning, as in that case the signal is largest and the beam spot remains a simple Gaussian. A square with a side of 200 pixels centered around the -1 order peak is then used as region of interest for all measurements of that run, as illustrated by the black dashed box in Figure 24. The region of interest is copied to the centre of a empty matrix with the same dimensions as the uncut measurement. The result is transformed back with the inverse Fourier transform and divided by the square root of the intensity of the rescaled reference beam. The resulting complex array is proportional to the electrical field of the signal beam, from which the intensity can be recovered by taking the absolute value squared and the phase by calculating the complex angle.

From the reconstructed intensity profiles, we can compute and normalise the transmission in the same way as in the previous Chapters. The result for a single run in shown in Figure 25a. Next to it an example of the reconstructed intensity profile at total absorption is shown. Interestingly, in the analysis, we did not see any ASE signal in the reconstructed intensity profile. This is to be expected, as the ASE is mostly generated in the optical amplifiers and thus the reference beam does not contain a significant ASE contribution. This means that the frequency components that are present in the signal beam due to ASE are not present in the reference beam and therefore do not lead to interference. It is important to note that even if there was ASE present in the reference beam, for instance because the amplifier or booster output was used to generate the reference beam, we would still not expect significant interference signal due to ASE unless the path length difference between the signal and reference beam
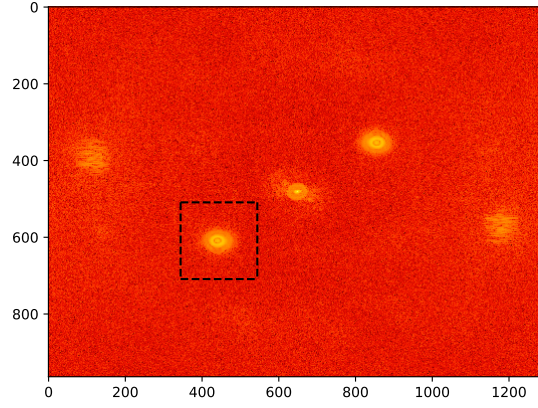
Figure 24: Fourier transform of a measurement after the rescaled reference beam has been removed. The black dashed lines forming a box indicate the region of interest in Fourier space.

would be less than the coherence length of the ASE, which is typically a few millimeters.
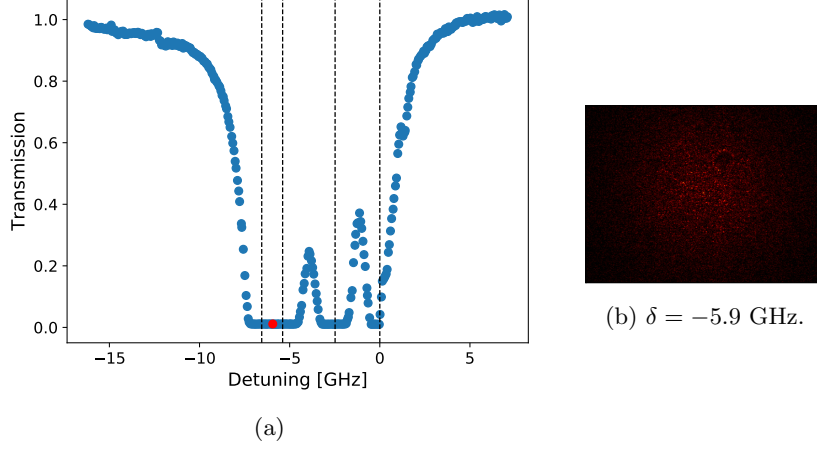
(b) $\delta = -5.9$ GHz.

(a)

Figure 25: Left the transmission measured with the off-axis holography setup at T=166 C$^\circ$ and $P_{\mathrm{in}} = 12$ mW. The red dot indicates the measurement corresponding to the image on the right (b).

4.4 Results

To quantify the quality of the off-axis measurements, we compare the transmission results with those obtained with the 'regular' direct intensity setup. We compare the off-axis transmission results with those of the camera without lens in the setup of Figure 8. We chose the camera setup without lens because the camera setup in the off-axis case also does not use lens(es).

We see that the transmission profiles are the very similar, but that in the off-axis case, we do resolve the detail in the branching pattern at the high detuning side. Secondly the off-axis graph shows a larger amount of noise in the form thin and short (single measurement) lines in many (arbitrary) places. This has the effect that the off-axis graph as a whole is much less smooth than the graph obtained with direct intensity measurement.

As mentioned before, the advantage of (digital) holography is the ability to reconstruct the electric field of a light signal, allowing the retrieval of both the intensity and phase from a single measurement. In Figure 27 two typical measurements of the phase and intensity are shown. The left column shows the intensity and the right column the corresponding phase. For the intensity images, red with an increasing brightness indicates an increasing intensity and for the phase images, white means a phase of zero while dark red/blue indicates +/- π respectively. In Figure 27a we see that the intensity profile forms a disk with a dark ring followed by a bright ring, while the corresponding phase shown next to it is a red disk surrounded by a blue ring followed by a red ring.

As for Figure 27c, the intensity profile shows a speckle-like pattern while the phase profile seems to consist of a broken disk surrounded by a ring pattern with breaks in some of the rings. These breaks are correspond to discontinuities
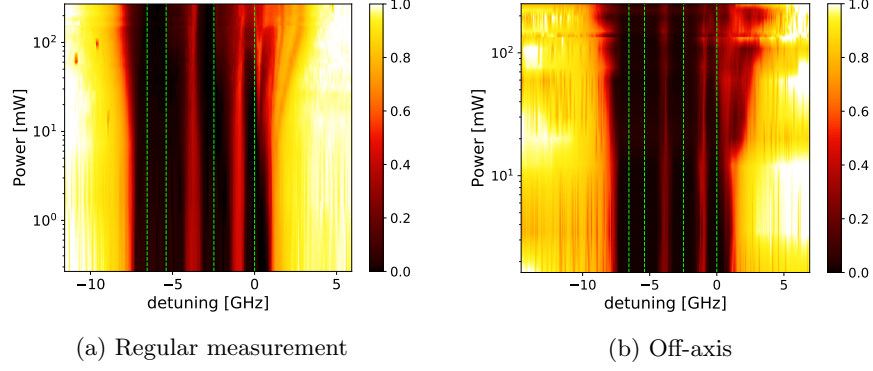
32

(a) Regular measurement   (b) Off-axis

Figure 26: Left (a), the transmission spectrum at T=164° as measured with a direct intensity setup using the camera without a lens and right (b) the transmission spectrum at T=166° as measured with the off-axis holography setup. Green dashed lines indicate the atomic transitions.
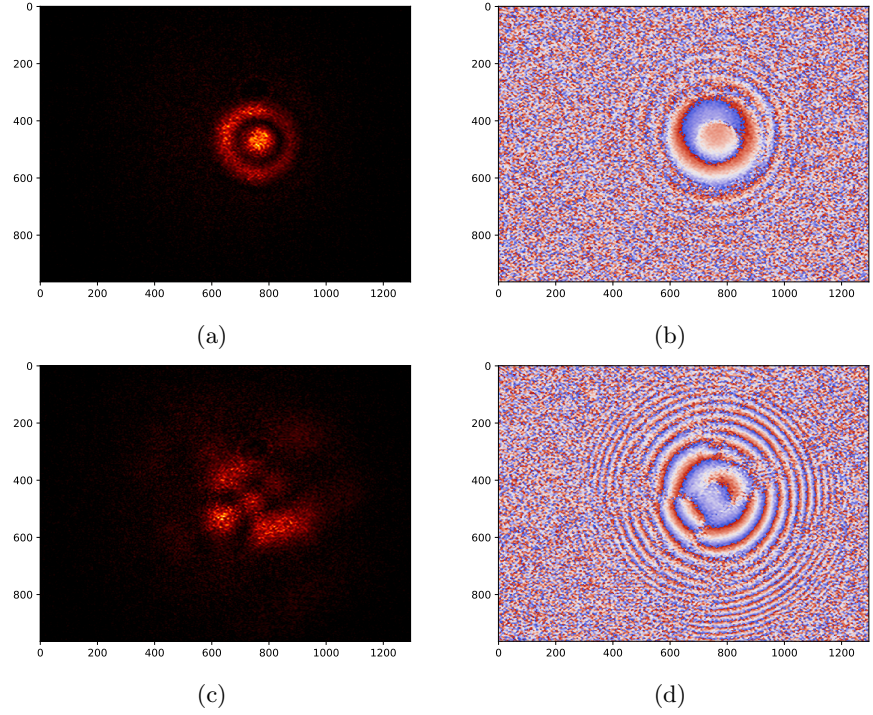

Figure 27: The left column shows the intensity of the reconstructed E-field while the right column shows the phase. For the top row $\delta = -3.8$ GHz and for the bottom row $\delta = 0.1$ GHz. All images were taken at T=166 °C and $P_{\text{in}} = 287$ mW.

of the phase. If we look carefully, these discontinuities seem to terminate into vertices.

4.5   Discussion

We have shown that by implementing off-axis holography and reconstructing the electric field from the interference pattern, the intensity and phase can be retrieved for a single measurement. Additionally, this method automatically filters the ASE from the signal and the resulting transmission spectra were shown to be consistent with those measured with regular intensity measurements. However, the amount of noise present in the measurements is such, that some features in the transmission spectrum become lost. This noise also makes the phase images somewhat difficult to interpret. This is probably caused by the higher complexity and sensitivity of off-axis holography measurements as compared with regular intensity measurements. This noise can likely be reduced by reducing the amount of vibrations in the setup and by using cameras with a higher shutter speed. Also, as mentioned in Chapter 3.2, if the NA is not sufficiently large, strongly refracting beams will not be fully captured on camera leading to branching and widening in the transmission plot as can be seen in Figure 26b. The NA therefore needs to be increased for future measurements in order to capture the full beam for all measurements.

Also, while we showed that intensity and phase profiles could be reconstructed, we have not been able to systematically analyse them. Future intensity measurements could be analysed with the structural similarity (SSIM) index, as was done in Chapter 3 for regular intensity measurements. However since the SSIM method is fitted to human perception, it will not be useful for characterising objects such as speckle patterns or, in the case of phase profiles, vortexes. As such, different and/or new methods of analysis would be necessary for such objects.

Lastly, with a single addition to the current setup, the evolution of the electric field through the vapour could be studied. If the amplitude and phase of the beam exiting the vapour cells are measured using off-axis holography, one could imprint this amplitude and phase onto the incident beam using a spatial light modulator (SLM). By repeating this process, measurements can be done virtually over any length that is a multiple of the cell length.

5   Conclusions and outlook

In conclusion this thesis successfully expanded upon van Lange's measurements on intense light in a dense Rubidium vapour by developing a setup that: probes over a larger frequency range, which includes multiple atomic transition lines, and that incorporates off-axis holography, which allows for the capture of both the intensity and the phase of a light beam.

The transmission measurements from the first setup are in good agreement with van Lange's measurements, except for those made at high vapour densities (see Chapter 2). Also, in the transmission spectra there were features, widening of the absorption at high vapour densities and P_{in}, branching absorption lines and the shifting and splitting of absorption minima, which could not be accounted for. However, both these features and discrepancy with van Lange's data was shown to disappear when the NA was increased (see Chapter 3.2), which means that they were a consequence of (part) of some beams falling outside the detection area of the camera.

A setup similar to that of van Lange, investigating beamshape behaviour over a large frequency range showed features reminiscent of van Lange's generalised detuning curve. Using van Lange's curve, and the data of beam profiles believed to be characteristic of these features, specific detuning curves describing these features could be calculated (see Chapter 3). These specific detuning curves were not only found to describe SSIM features at frequencies above resonance, where van Lange measured, but also described some features at frequencies beneath resonance. This shows that on both sides of an atomic resonance the physics determining beam profiles is similar.

Beam profiles with no features which could be described by the generalised detuning curve were also identified. One cause may be that the SSIM method, which mimics human perception, is unable to distinguish well between certain beam profiles, such as beam profiles differing slightly from a Gaussian profile, speckle profiles, and noisy beam profiles. An other likely cause for the generalised detuning curve being an unfit description for some beam profiles would be that, when the optical frequency gets close to multiple transition lines, the physics responsible for the beamshape is affected, necessitating a description different from the general detuning curve. The SSIM method is not suitable to characterise beamshapes in regions with multiple close transtion lines due to the appearance of speckle and noisy profiles in that area. Other methods therefore need to be used or developed to investigate behaviour influenced by multiple transition lines.

Preliminary measurements with the off-axis holography setup showed that phase and intensity could be captured simultaneously. However, when off-axis transmission measurements were compared to regular intensity measurements of the transmission, the former showed a greater amount of noise. This is probably due to the greater complexity and sensitivity of such measurements, and for future measurements a greater control of vibrations in the experimental setup and usage of cameras with higher shutter speed are therefore recommended. Additionally, in this thesis no methods to investigate phase profiles have been

put forward, and as the phase is an important property of a light beam, such methods need to be explored for future measurements. Lastly, the off-axis setup can be improved to also measure beam profiles as a function of cell length, this can be done with the addition of a spatial light modulator (SLM) in front of the cell, which would be used to create a beam at the cell entrance with the same amplitude and phase as the beam measured at the cell exit.

A   Background and ASE

In Chapter 2 Figure 3a, we saw a transmission spectrum which showed a transmission of 29% where total absorption was expected. We attributed this to amplified spontaneous emission (ASE). But an ASE that is 29% of the signal is unexpectedly high and would mean that a large portion of P_{in} is wasted on the ASE instead of being used for the measured optical frequency. Possibly transmission considered to be part of the ASE is due to noise or background that has not been taken into account, therefore here a closer look is taken at the ASE and background.

In order to test whether or not the ASE is as high as initially thought, two new methods to determine the ASE were used. In the first method, a Gaussian profile is fitted to the first (far detuned) frame. The position and the width of the peak found with this fit, are used to define a square area. The peak is used as centre, and the length of the sides of the square are chosen to be two times the width of the Gaussian profile. Subsequently for every frame the background is subtracted as described in Chapter 2.2. After this, only those pixels inside the area defined by the square are summed to calculate the transmission. Note that transmission spectra measured this way, will be distorted for measurements where the beam shape changes or moves enough to make it fall outside of the defined square. This is not a problem for ASE measurements since the ASE is in the same position and has the same shape as the signal.

For the other method, 20 frames with total absorption are determined from the transmission spectrum. The background of each frame is subtracted, after which a Gaussian profile is fitted to the each image. The same is done for the first and last 10 frames (far detuned beams on both sides of the spectrum) of that run. The fitted Gaussians are discretised back on the pixel grid and then summed over the pixels. The relative strength of the ASE is then determined by dividing the results found at total absorption by the average results found in the far detuned cases.

Figure 28 shows the results of the different methods as measured with the setup of Figure 8 for $T = 175 \ C^{\circ}$. The top left graph shows results after normalisation, but without background subtraction. The 'regular' camera is named cam1 in the plots, and it measures an average background of 12% of the maximum signal while for cam2, the Fourier camera, the background is 41% of the maximum signal. The graph next to it (top right) shows the result after the background subtraction. This results in an ASE that is equal to 10% of the signal for the regular camera and an ASE of 19% of the signal for the Fourier camera. Since both cameras are measuring the same ASE this large difference in values means that there is still background present. In the second row, the results of the new methods are shown, with on the left side those of the small area sum and on the right those of the Gaussian fits. For both methods the results from both cameras are very close, 10% for the regular camera and 9% for the Fourier camera. This strongly suggests that what is measured is the actual ASE.
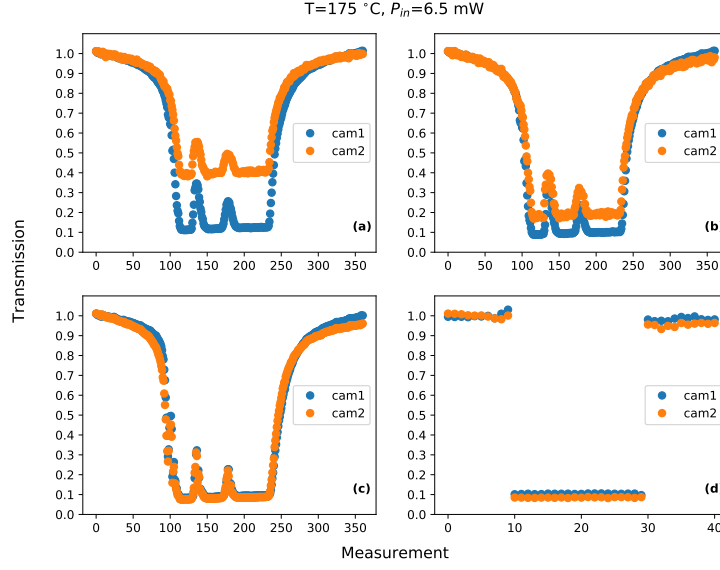
Figure 28: Plots show transmission of the same run made with the setup in Figure 8, blue for regular camera and orange for Fourier camera, with T=175 °C and P_{in} = 6.5 mW. Different measurements indicate different optical frequencies. In (a) the normalised transmission without background subtraction is shown. In (b) the normalised transmission is shown after background subtraction. In (c) the transmission calculated, after background subtraction, from a square area determined by a Gaussian fit is shown. In (d) the transmission calculated, after background subtraction, from a Gaussian profile fitted to each of the measurements is shown. The 40 measurements shown in (d) are; 10 far detuned measurements on both the negative and positive side, and in the middle 20 measurements with total absorption.

These new methods to calculate the ASE were subsequently used for all of the measurements done with the setup in Figure 8. From these, the average ASE was calculated for every run, the results of which are shown in Figure 29. Because both methods gave the same results, only the results from the reduced area method is shown. Note that while a change in run number corresponds to a change in P_{in}, the same run numbers for different vapour temperatures do not necessarily correspond to the same P_{in}. In the Figure we can see that the ASE for T=175 °C and T=185 °C fluctuates around 12% and 13% respectively. While for T=164 °C the ASE is close to 5% and the fluctuations are are also much smaller. It is unknown what caused these differences.

The actual input power P_{in} for the frequency measured is the power measured in front of the vapour cell, minus the part of that power that is due to the ASE. If the relative power of the ASE would remain largely constant between runs, all the P_{in} measurements would need to be multiplied by the same factor. The large fluctuations in relative ASE power we measured, however, would
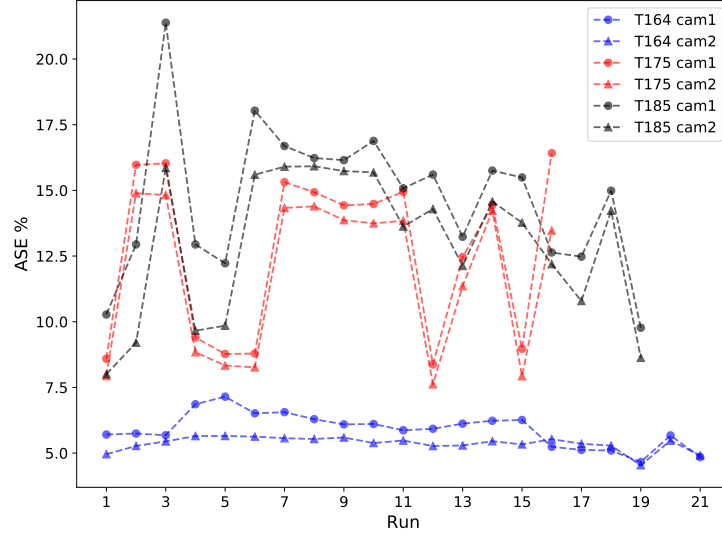
38

Figure 29: The average ASE power as percentage of the maximal signal power for different runs and vapour temperatures.

mean that the measured P_{in} for every run needs to be multiplied by a different factor to get the correct input power for the measured frequency. Although this makes measurements more complicated, getting the correct input power is still possible, the relative strength of the ASE just needs to be measured for every run. However the methods we used to measure the relative power of the ASE can only be applied to runs with total absorption. This is problematic for measurements at lower vapour temperatures since there runs with high P_{in} will have no total absorption.

We have therefore not been able to compensate the measured input power with that of the ASE, which has consequences for quantitative comparisons of measurements, since this shows that different runs, which should have the same input power, could have actually be done at different input powers. Therefore, for future experiments, methods should be developed to remove the ASE or at least keep its power relative to the signal constant.

References

[1] Mario Bertolotti. *The history of the laser.* CRC press, 2004.

[2] W. Kaiser and C. G. B. Garrett. Two-photon excitation in CaF_2: Eu^{2+}. *Phys. Rev. Lett.*, 7:229–231, Sep 1961.

[3] P. A. Franken, A. E. Hill, C. W. Peters, and G. Weinreich. Generation of optical harmonics. *Phys. Rev. Lett.*, 7:118–119, Aug 1961.

[4] Lene Vestergaard Hau, Stephen E Harris, Zachary Dutton, and Cyrus H Behroozi. Light speed reduction to 17 metres per second in an ultracold atomic gas. *Nature*, 397(6720):594–598, 1999.

[5] Christopher Slowe, Naomi S. Ginsberg, Trygve Ristroph, Anne Goodsell, and Lene Vestergaard Hau. Ultraslow light & bose-einstein condensates: Two-way control with coherent light & atom fields. *Opt. Photon. News*, 16(5):30–34, May 2005.

[6] Lucas Schweickert, Klaus D Jöns, Mehdi Namazi, Guodong Cui, Thomas Lettner, Katharina D Zeuner, Lara Scavuzzo Montana, Saimon Filipe Covre da Silva, Marcus Reindl, Huiying Huang, et al. Electromagnetically induced transparency of on-demand single photons in a hybrid quantum network. *arXiv preprint arXiv:1808.05921*, 2018.

[7] J. D. Siverns, J. Hannegan, and Q. Quraishi. Demonstration of slow light in rubidium vapor using single photons from a trapped ion. *Science Advances*, 5(10), 2019.

[8] Michael Fleischhauer, Atac Imamoglu, and Jonathan P. Marangos. Electromagnetically induced transparency: Optics in coherent media. *Rev. Mod. Phys.*, 77:633–673, Jul 2005.

[9] Stephen E. Harris. Electromagnetically induced transparency. *Physics Today*, 50:36–42, Jul 1997.

[10] Q. Fontaine, T. Bienaimé, S. Pigeon, E. Giacobino, A. Bramati, and Q. Glorieux. Observation of the bogoliubov dispersion in a fluid of light. *Phys. Rev. Lett.*, 121:183604, Oct 2018.

[11] Neven Šantić, Adrien Fusaro, Sabeur Salem, Josselin Garnier, Antonio Picozzi, and Robin Kaiser. Nonequilibrium precondensation of classical waves in two dimensions propagating through atomic vapors. *Phys. Rev. Lett.*, 120:055301, Feb 2018.

[12] Jon D Swaim, Kaitlyn N David, Erin M Knutson, Christian Rios, Onur Danaci, and Ryan T Glasser. Atomic vapor as a source of tunable, non-gaussian self-reconstructing optical modes. *Scientific reports*, 7:42311, 2017.

[13] Qian Zhang, Xuemei Cheng, Bo He, Haowei Chen, Zhaoyu Ren, and Jintao Bai. Size-variable dark-hollow beam generation using cross-phase modulation. *Optics & Laser Technology*, 119:105582, 2019.

[14] Arie Johannes van Lange. *Non-linear optical effects in cold and hot rubidium gases*. PhD thesis, Utrecht University, Utrecht, The Netherlands, 2020.

[15] James Keaveney. *Cooperative interactions in dense thermal Rb vapour confined in nm-scale cells*. PhD thesis, Department of Physics, Durham University, South Road, Durham, DH1 3LE, UK, 2013.

[16] Zhou Wang, A. C. Bovik, H. R. Sheikh, and E. P. Simoncelli. Image quality assessment: from error visibility to structural similarity. *IEEE Transactions on Image Processing*, 13(4):600–612, 2004.

[17] S van der Walt, JL Schönberger, J Nunez-Iglesias, F Boulogne, JD Warner, N Yager, E Gouillart, T Yu, and the scikit-image contributors. scikit-image: Image processing in python. *PeerJ*, 2:e453, 2014.

[18] Emmett N. Leith and Juris Upatnieks. Reconstructed wavefronts and communication theory. *J. Opt. Soc. Am.*, 52(10):1123–1130, Oct 1962.

[19] Mitsuo Takeda, Hideki Ina, and Seiji Kobayashi. Fourier-transform method of fringe-pattern analysis for computer-based topography and interferometry. *J. Opt. Soc. Am.*, 72(1):156–160, Jan 1982.

[20] Etienne Cuche, Pierre Marquet, and Christian Depeursinge. Spatial filtering for zero-order and twin-image elimination in digital off-axis holography. *Appl. Opt.*, 39(23):4070–4075, Aug 2000.